

CrossMark
click for updatesCite this: *J. Mater. Chem. A*, 2015, 3, 19850

An electrospun hierarchical LiV_3O_8 nanowire-in-network for high-rate and long-life lithium batteries†

Wenhao Ren,[‡] Zhiping Zheng,[‡] Yanzhu Luo, Wei Chen,* Chaojiang Niu, Kangning Zhao, Mengyu Yan, Lei Zhang, Jiashen Meng and Liqiang Mai*

Structural and morphological control of the LiV_3O_8 material has a significant impact on its electrochemical performance. In order to obtain a favorable structure, a hierarchical LiV_3O_8 nanowire-in-network is designed and constructed by electrospinning through a polymer crosslinking strategy. The crosslinking effect between poly(vinyl alcohol) (PVA) and poly(ethylene oxide) (PEO) not only benefits electrospinning, but also realizes a mild multi-step degradation process during calcination. Based on temperature-dependent experiments and thermogravimetric (TG) analysis, the function of polymer blends and the formation mechanism of the structure are discussed in detail. As a cathode for lithium batteries, LiV_3O_8 exhibits a high initial capacity of $320.6 \text{ mA h g}^{-1}$ at 100 mA g^{-1} and a high-rate capacity of $202.8 \text{ mA h g}^{-1}$ at 2000 mA g^{-1} . This remarkable performance is attributed to its unique structure, which provides a large effective contact area, low charge transfer resistance, and improved structural stability. Our work indicates that the hierarchical LiV_3O_8 nanowire-in-network material is a promising cathode for use in high-rate and long-life rechargeable lithium batteries.

Received 24th June 2015
Accepted 17th August 2015

DOI: 10.1039/c5ta04643b

www.rsc.org/MaterialsA

Introduction

Lithium batteries (LBs) have attracted extensive attention in portable electronic devices and electric vehicles owing to their high energy density and long cycle life. For further widespread application, significant efforts should be made to reduce the cost and improve the electrochemical performance.^{1–10} The layered lithium trivanadate (LiV_3O_8) cathode material has attracted considerable attention due to its low cost, abundant sources, high energy density, and good safety features.^{11–15} Although a variety of methods have been developed for the synthesis of LiV_3O_8 in recent years, it still suffers from unsatisfactory capacity loss and poor rate capability because of the incomplete phase transformation, slow electrode kinetics, and structural degradation.^{16–21}

It has been reported that the electrochemical performance of LiV_3O_8 is influenced by its morphology significantly.²² The rational design of LiV_3O_8 with a favorable structure is of great importance. Nanostructured materials with specific

architecture such as hierarchical nanowires not only provide extra tunnels for fast ion diffusion, but also effectively prevent the self-aggregation of nanomaterials during charge/discharge processes. Furthermore, the formation of a network structure can further improve the stability and electronic conduction of hierarchical nanowires.^{23–25} Therefore, the network architecture consisting of hierarchical nanowires is a favorable structure for high performance lithium batteries.

It is worth noting that electrospinning has been widely recognized as a convenient and cost-effective method to generate a variety of nanowires with unique morphologies.^{26–29} However, a typical electrospinning technique could only obtain nanowires with a simple morphology and the design of a unique structure is still a challenge. Herein, we propose a crosslinking strategy *via* controlled electrospinning to construct a hierarchical LiV_3O_8 nanowire-in-network. This strategy takes advantage of the characteristics of different polymers, which influence spinning performance and pyrolysis features. Based on the method, a mild multi-step degradation process during calcination is achieved, thus in favor of the formation of the structure. The continuous morphological development of LiV_3O_8 (Fig. 1) mainly includes three stages, from smooth nanofibers to hierarchical nanowires, and finally a nanowire-in-network structure. This unique architecture can provide continuous electronic conduction and extra tunnels for efficient contact between LiV_3O_8 and electrolytes, affording low charge transfer resistance and high specific capacity. It is expected that the crosslinking strategy in electrospinning could be extended

State Key Laboratory of Advanced Technology for Materials Synthesis and Processing, Wuhan University of Technology, Hubei, Wuhan 430070, China. E-mail: mlq518@whut.edu.cn; chenwei_juan@sina.com

† Electronic supplementary information (ESI) available: FTIR spectra, TEM images, SAED patterns, FESEM images, and TG images of the samples, charge-discharge curves and differential capacity vs. voltage curves of LVO-PVA/PEO at different cycles, and related photographs of the synthesis processes of the samples. See DOI: 10.1039/c5ta04643b

‡ These authors contributed equally to this work.

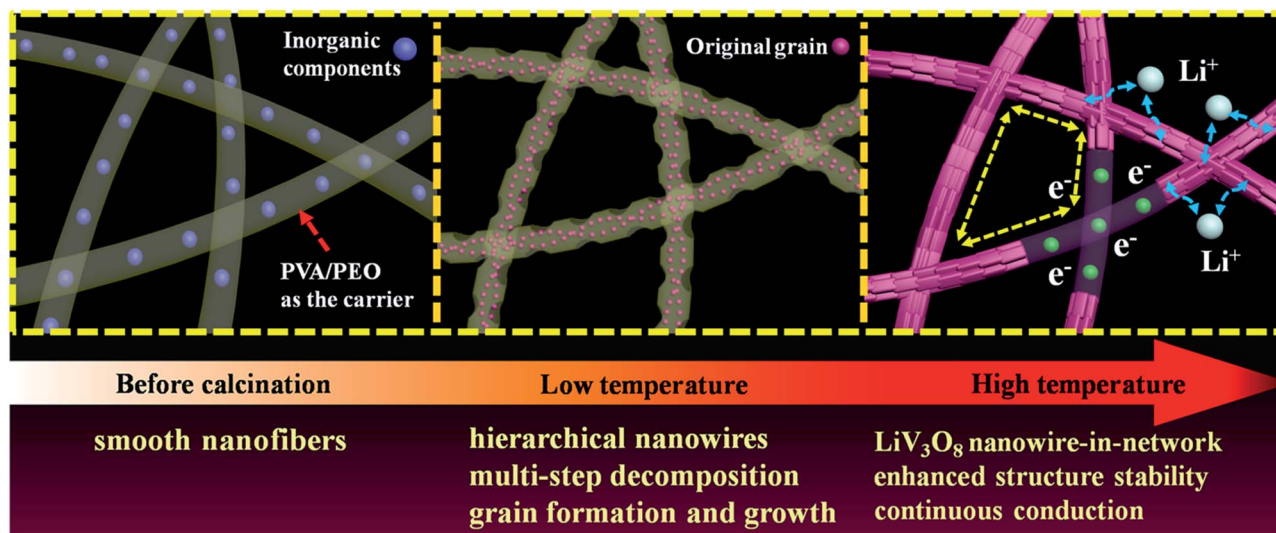


Fig. 1 Schematic illustration of the proposed formation mechanism of the hierarchical LiV_3O_8 nanowire-in-network during calcination.

to the preparation of other nanomaterials with unique architectures.

Experimental section

Materials synthesis

For a typical synthesis, ammonium metavanadate (NH_4VO_3 , 0.528 g), lithium acetate (LiAc, 0.161 g), PEO (0.9 g, $M_w = 400\,000$), and PVA (0.9 g, $M_w \approx 65\,000$) were dissolved in 30 mL distilled water with stirring at $80\text{ }^\circ\text{C}$ for 6 h. A light-yellow clear solution was obtained with a certain viscosity. Then, the precursor solution was loaded into a plastic syringe and injected at a constant flow rate of 0.5 mL h^{-1} . The spinning voltage was set at 20 kV and the distance between the collector and the spinneret was 15 cm. Finally, the as-prepared nanofibers with aluminum foil were annealed at $400\text{ }^\circ\text{C}$ in air for 5 h to obtain a brown powder. For comparison, the samples were also synthesized by using PVA or PEO individually. The final products synthesized through PVA, PEO, or PVA/PEO were marked as LVO-PVA, LVO-PEO, and LVO-PVA/PEO, respectively.

Materials characterization

X-ray diffraction (XRD) measurements were performed to investigate the crystallographic information using a D8 Advance X-ray diffractometer with a non-monochromated $\text{Cu K}\alpha$ X-ray source. Fourier transformed infrared (FTIR) transmittance spectra were recorded using a 60-SXB IR spectrometer. Field emission scanning electron microscopy (FESEM) images were collected with a JEOL JSM-7100F at an acceleration voltage of 10 kV. Transmission electron microscopy (TEM) and high-resolution TEM (HRTEM) images were recorded with a JEM-2100F microscope. TG analysis was performed using a NETZSCH-STA449c/3/G thermoanalyzer.

Electrochemical measurements

The electrochemical measurements were performed with 2025 coin cells assembled in a glovebox filled with pure argon.

Lithium foil was used as the anode and 1 M solution of LiPF_6 in ethylene carbon (EC)/dimethyl carbonate (DMC) was used as the electrolyte. Cathode electrodes were produced with a 70 wt% LiV_3O_8 active material, 20 wt% acetylene black and 10 wt% poly(tetrafluoroethylene) (PTFE). The battery was aged for 24 h before the test to ensure full absorption of the electrolyte into the electrodes. The mass loading of the active material was $3\text{--}4\text{ mg cm}^{-2}$. Galvanostatic charge/discharge measurements were performed in the potential range from 1.5 to 4 V vs. Li/Li^+ with a multichannel battery testing system (LAND CT2001A). Cyclic voltammetry (CV) and electrochemical impedance spectroscopy (EIS) were performed with an electrochemical workstation (Autolab PGSTAT302N).

Results and discussion

The XRD measurements were conducted to determine the phase structures of the samples. As shown in Fig. 2a, all the prepared materials are indexed to the layered monoclinic LiV_3O_8 phase (JCPDS card no. 72-1193, space group: $P2_1/m$), which is consistent with previous reports.^{13,30} Moreover, the peak positions and the peak intensities of sample LVO-PVA, LVO-PEO, and LVO-PVA/PEO are similar, suggesting that the polymer component does not significantly change the crystal structure of LiV_3O_8 . Then, FTIR spectroscopy of LVO-PVA/PEO was applied to further investigate the structural change in bonding (Fig. 2b). Before annealing, the strong bands observed between 500 and 2000 cm^{-1} can be assigned to bending and stretching vibrations of PVA and PEO. The band at 2888 cm^{-1} is attributed to the vibrations of $-\text{CH}_2-$.¹⁴ Notably, the hydroxyl stretching band of LVO-PVA/PEO at 3416 cm^{-1} is higher than that of LVO-PVA at 3400 cm^{-1} but lower than that of LVO-PEO at 3431 cm^{-1} (Fig. S2,†), indicating that the intra- and intermolecular interactions among PVA have been weakened by crosslinking with PEO and the newly formed hydrogen bonds are stronger.³¹ After annealing, the bands belonging to PVA and PEO disappeared; instead, well defined features of LiV_3O_8 are

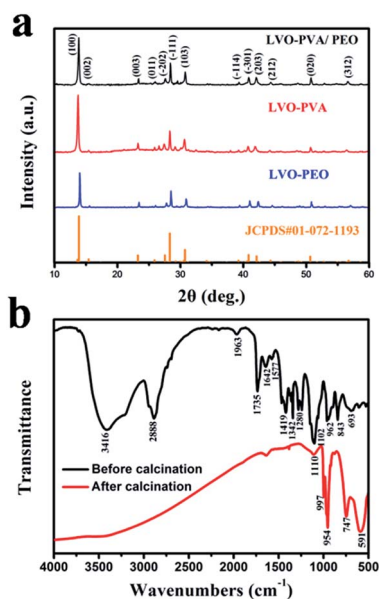


Fig. 2 (a) XRD patterns of LVO-PVA/PEO, LVO-PVA, and LVO-PEO. (b) FTIR spectra of the electrospun LVO-PVA/PEO composite before and after calcination.

observed. The bands at 997 and 954 cm^{-1} are assigned to the vibrations of $\text{V}=\text{O}$. The band at 747 cm^{-1} is attributed to the stretching vibrations of $\text{V}-\text{O}-\text{V}$ and peaks between 600 and 400 cm^{-1} are attributed to the bending vibrations of $\text{V}-\text{O}-\text{V}$ and $\text{V}=\text{O}$.^{17,32,33}

SEM and TEM were used to characterize the morphology and detailed structure of the samples. Fig. 3 shows the SEM images of electrospun nanofibers of LVO-PVA/PEO, LVO-PVA, and LVO-PEO before and after calcination at 400 °C. All the electrospun nanofibers are smooth and uniform before annealing; the

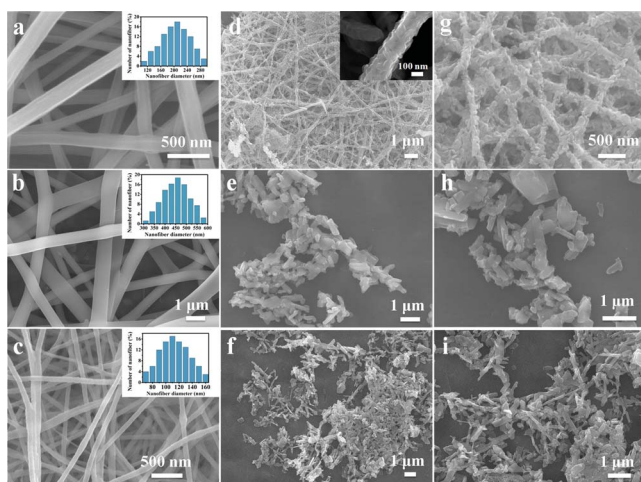


Fig. 3 SEM images of electrospun LVO-PVA/PEO (a), LVO-PVA (b) and LVO-PEO (c) before annealing. The insets of (a–c) are the corresponding diameter distribution diagrams. SEM images of LVO-PVA/PEO (d and g), LVO-PVA (e and h) and LVO-PEO (f and i) after annealing. The inset of (d) is the SEM image of a single LVO-PVA/PEO nanowire.

diameter distribution of LVO-PVA/PEO, LVO-PVA, and LVO-PEO is centered at 200, 450, and 110 nm, respectively. Notably, the diameter of electrospun nanowires decreases with the increment of the PEO content. This is because the addition of PEO can weaken the hydrogen bonds in PVA molecules, thus inhibiting crystallization and increasing the nucleation points of PVA, which therefore promotes the movability of PVA molecular chains under an electrostatic force.³¹

Interestingly, only LVO-PVA/PEO can form a hierarchical nanowire-in-network structure after heat-treatment. The length of the nanowires is up to several millimeters; the width and length of each attached nanorod are around 50 and 150 nm, respectively. However, the morphologies of LVO-PVA and LVO-PEO are self-aggregated and mainly composed of detached nanorods with an irregular structure. An irregular morphology similar to that of LVO-PVA has also been reported by Kwang-Pill Lee *et al.* via electrospinning.³⁴ TEM images show that the LVO-PVA/PEO nanowires and nanorods (Fig. 4a and b) are tightly connected with each other. The Fast Fourier Transformation (FFT) patterns (Fig. 4d) indicate that the edge of nanowires is single-crystalline and well-defined in the crystal phase. Fig. 4e also reveals that there exist two sets of lattices in the connected region and further confirms that the particles have grown together and formed the grain. The lattice spacing of 11.52 Å shown in the HRTEM image (Fig. S3†) corresponds to the (001) interplanar distance of LiV_3O_8 (JCPDS card no. 72-1193). The SAED pattern reveals the well-defined orientation of the nanorod and the axial direction is $[\bar{3}01]$.

Most importantly, unlike typical preparation for sol precursors that is only based on one sort of polymer (PVA, PVP or PEO, *etc.*), we select two complementary polymers to achieve a better electrospinning process. On the one hand, the use of PVA can promote both the electrical conductivity of the solution and the mechanical properties of spinning. However, the melting point of PVA is close to its decomposition temperature, resulting in poor processability and a fierce decomposition process. Besides, PVA molecules possess high hydrophilicity, and a high concentration of PVA solution seriously affects solvent volatilization and is easy to separate out during electrospinning.^{35,36} On the other hand, the addition of PEO can weaken the intra- and inter-molecular hydrogen bonds of PVA, change the aggregation states of PVA chains, and decrease its melting point and crystallinity. Then the movability of PVA molecular chains is promoted and becomes liable to extend under the outside force. Thus, the polymer blends are favorable for the formation of spinning and the diameter of electrospun nanofibers becomes smaller.^{31,37,38} Moreover, PVA and PEO also served as carriers and effectively prevented the self-aggregation of the nanorods during the heat-treatment process.

Although some similar formation mechanisms were investigated by other researchers,³⁹ the function of polymer blends for constructing a hierarchical structure was ignored. Therefore, the temperature-dependent experiments combined with TG analysis were conducted to gain further insight into the formation mechanism of the LiV_3O_8 network structure. The continuous morphological evolution of sample LVO-PVA/PEO (Fig. 1) mainly includes three stages, from smooth nanofibers to

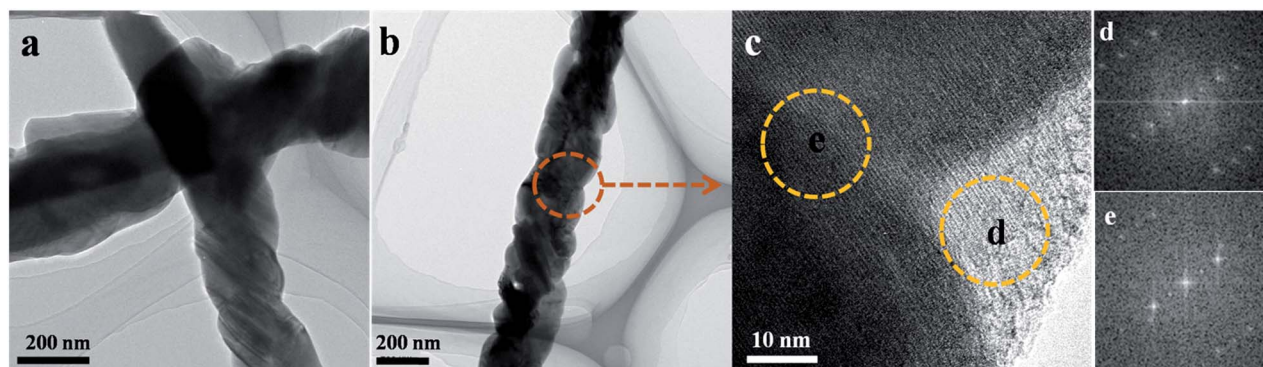


Fig. 4 TEM images (a and b), HRTEM image (c) and FFT patterns (d and e) of hierarchical LVO-PVA/PEO nanowires.

hierarchical nanowires, and finally a nanowire-in-network structure. In the first stage, the smooth nanofibers start to degrade and become rough. A mass loss of about 7.56 wt% is observed on the TG curve (Fig. 5a) from 100 °C to 170 °C due to the oxidation and dehydration of the electrospun LVO-PVA/PEO composite. The first two peaks indicated by differential scanning calorimetry (DSC) at 67 °C and 150 °C are attributed to the T_m (melting temperature) and initial degradation of PVA. In the second stage, the nucleation of the original LiV_3O_8 grain and the decomposition of polymers occur simultaneously so that hierarchical nanowires are formed (Fig. S4†). The composite was further oxidized with a 51.47 wt% mass loss from 170 °C to 265 °C. This mass loss is mainly attributed to the decomposition of PVA as can be deduced from the DSC curve of LVO-PVA (Fig. 5b, red curve). Notably, the DSC peak of LVO-PVA at 253 °C is much higher than that of LVO-PVA/PEO at 240 °C. Thus, the reaction intensity of LVO-PVA/PEO becomes mild due to the use of PEO. Besides, PEO is still stable at this stage and helps to maintain the basic structure of LVO-PVA/PEO, so that the decomposition of PVA would not destroy the structure significantly. In the third stage, the small LiV_3O_8 particles gradually grow into connected nanorods and replace polymer components as the carrier for constructing a hierarchical nanowire-in-network structure. The 18.51 wt% mass loss from 265 °C to 445 °C is due to the complete decomposition of polymers. Similarly, the reaction intensity of LVO-PVA/PEO is lower than that of LVO-PEO in this temperature interval. As the calcination temperature increased to 450 °C, the size of LiV_3O_8 nanorods grows much bigger and it consumes a large number of connected materials. Thus the self-aggregation of nanorods occurs and the hierarchical nanowire-in-network structure cannot be maintained (Fig. S5†). In summary, only LVO-PVA/PEO can form the unique hierarchical structure under controlled calcination. This is attributed to the different pyrolysis properties of PVA and PEO; thus a mild multi-step degradation process is achieved *via* polymer crosslinking; in this way a gentle heat-treatment process is ensured.

Detailed electrochemical measurements were conducted to investigate the lithium storage performance. Fig. 6a shows the cyclic voltammetry curve of LVO-PVA/PEO calcined at 400 °C. The voltammograms were measured at a sweep rate of 0.1 mV s^{-1} in the potential window of 1.5 to 4.0 V at room temperature.

All of these peaks originate from the phase transitions between $\text{Li}_{1+x}\text{V}_3\text{O}_8$ components with different x values ($0 < x < 3$). The cathodic peak at 3.59 V corresponds to the initial Li ion insertion into the octahedral site of the LiV_3O_8 host structure. The small peak at 2.67 V corresponds to Li ion insertion into the empty tetrahedral site through a single-phase reaction. Pan *et al.*¹¹ reported a similar phenomenon that the rod-shape LiV_3O_8 has relatively low peak intensity at this potential. The peak at 2.38 V is related to the filling of octahedral sites formed upon intercalation during which a two-phase transition from $\text{Li}_3\text{V}_3\text{O}_8$ to $\text{Li}_4\text{V}_3\text{O}_8$ occurs. The last step at 2.05 V is attributed to the slower kinetic insertion process where the single-phase transition corresponding to the $\text{Li}_4\text{V}_3\text{O}_8$ phase takes place and all of the lithium ions are octahedrally coordinated.^{30,40} When comparing the initial three cycles of the CV curves, the partial irreversibility of phase transformation between the $\text{Li}_4\text{V}_3\text{O}_8$ and the $\text{Li}_3\text{V}_3\text{O}_8$ phases at 2.38 V caused a decrease in the discharge capacity, leading to capacity decay during cycling. Lithium insertion kinetics of $\text{Li}_{1+x}\text{V}_3\text{O}_8$ is affected largely by the small diffusivity of Li ions in the $\text{Li}_4\text{V}_3\text{O}_8$ phase formed for $x > 1.5$ upon lithiation.⁴¹

Fig. 6b displays the initial charge–discharge curves of LVO-PVA/PEO, LVO-PVA, and LVO-PEO cathodes measured at 100 mA g^{-1} in the range of 1.5–4.0 V. Sample LVO-PVA/PEO shows the highest discharge capacity (320 mA h g^{-1}) which benefits from the hierarchical structure. Several plateaus are found because of diverse phase transformations within the electrode materials during Li ion insertion/extraction. Three discharge plateaus located around 2.80, 2.65 and 2.20 V can be identified due to the insertion of Li ions, which result from the single-phase insertion process, the two-phase transformation from $\text{Li}_3\text{V}_3\text{O}_8$ to $\text{Li}_4\text{V}_3\text{O}_8$ and the slower kinetic insertion process, respectively. Essential information on the anodic/cathodic processes in the LiV_3O_8 electrodes can be extracted from the charge/discharge curves by translation into differential capacity curves (Fig. S8†). The anodic and cathodic peak intensities remain relatively stable after cycling. The major capacity decay is due to the partial irreversibility of phase transformation between the $\text{Li}_4\text{V}_3\text{O}_8$ and the $\text{Li}_3\text{V}_3\text{O}_8$ phases which is consistent with the CV results.

Fig. 7 shows the cycling performances of three samples measured at various current densities (100, 1000 and 2000 mA

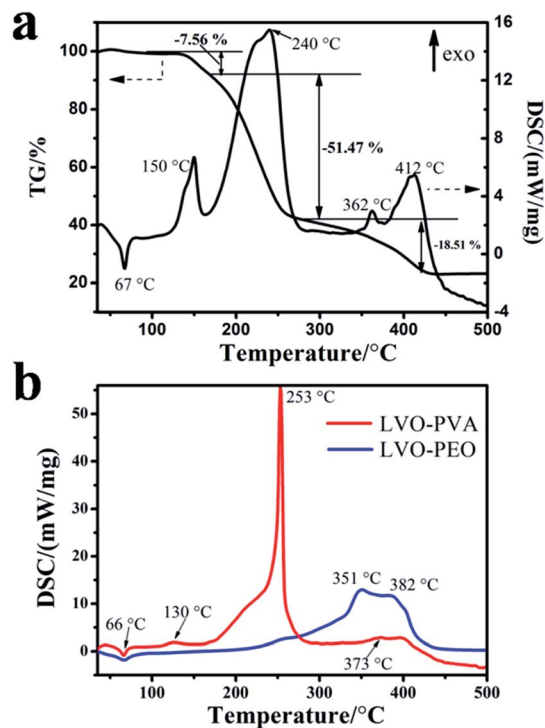


Fig. 5 (a) TG and DSC curves of the electrospun LVO-PVA/PEO composite. (b) DSC curves of the electrospun LVO-PVA and LVO-PEO composite.

g^{-1}). At a current density of 100 mA g^{-1} , the initial discharge capacity of sample LVO-PVA/PEO is up to $320.6 \text{ mA h g}^{-1}$, higher than that of LVO-PVA ($284.3 \text{ mA h g}^{-1}$) and LVO-PEO ($246.8 \text{ mA h g}^{-1}$). This is attributed to the large effective contact area provided by the hierarchical structure. After 100 cycles, the discharge capacities decreased to 271.7 , 231.3 and $157.1 \text{ mA h g}^{-1}$, corresponding to the capacity retention of 84.7% , 81.3% and 63.6% , respectively. The cycling performance of these three samples at a high current density is further investigated. When cycled at 1000 mA g^{-1} , compared with LVO-PVA ($207.2 \text{ mA h g}^{-1}$) and LVO-PEO ($179.2 \text{ mA h g}^{-1}$), the LVO-PVA/PEO cathode exhibits a remarkable initial capacity of $254.0 \text{ mA h g}^{-1}$. After 500 cycles, the LVO-PVA/PEO cathode still delivers a discharge capacity of $129.1 \text{ mA h g}^{-1}$, almost two times that of the LVO-PEO cathode (64.8 mA h g^{-1}). When the current density increases to 2000 mA g^{-1} , the initial discharge capacity of LVO-PVA/PEO, LVO-PVA and LVO-PEO is 202.8 , 154.5 , $159.4 \text{ mA h g}^{-1}$, respectively. It is worth noting that the LVO-PVA/PEO cathode exhibits a remarkable capacity of $102.7 \text{ mA h g}^{-1}$ after 500 cycles, much higher than that of LVO-PVA (69.5 mA h g^{-1}) and LVO-PEO (57.2 mA h g^{-1}) cathodes, indicating its excellent high-rate capability. Obviously, the LVO-PVA/PEO electrode exhibits the highest capacity and best cycling performance at both low and high current densities. Fig. 7d shows the rate performance of LVO-PVA/PEO from 100 to 2000 mA g^{-1} . Notably, the electrode shows stable capacities in each state and still provides a specific discharge capacity of 110 mA h g^{-1} even at 2000 mA g^{-1} . When the rate is turned back to 100 mA g^{-1} , a specific discharge capacity of $274.8 \text{ mA h g}^{-1}$ still can be

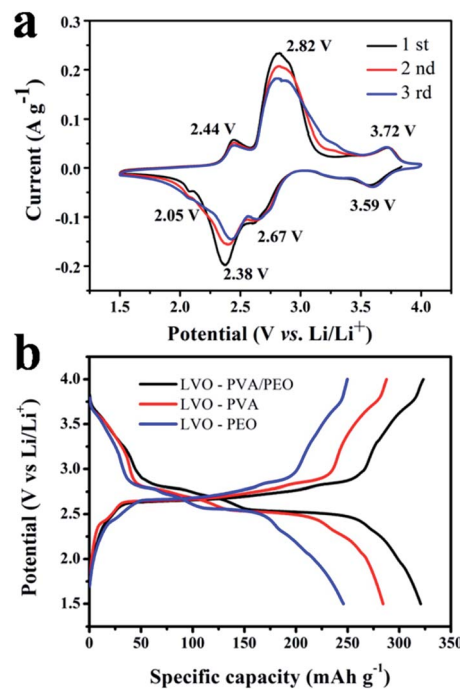


Fig. 6 (a) The CV curves of LVO-PVA/PEO at a sweep rate of 0.1 mV s^{-1} in the potential range from 1.5 to $4.0 \text{ V vs. Li/Li}^+$. (b) Charge-discharge curves of LVO-PVA/PEO, LVO-PVA and LVO-PEO at 100 mA g^{-1} .

obtained, indicating the robust structural stability. The lithium storage performance of recently published LiV_3O_8 based cathode materials is summarized in Table S1.†

The advantage of the hierarchical nanowire-in-network structure is further verified by the comparison of the EIS results of LVO-PVA/PEO, LVO-PVA, and LVO-PEO electrodes. Before the EIS test, the cells were charged to 3.0 V and then kept at that voltage for a period of time to reach a stable state. The Nyquist plots (Fig. 8a) exhibit two semicircles in the high frequency and medium frequency regions. The high frequency semicircle is related to the interface parameters such as surface film contribution and solid-electrolyte inter-phase resistance. The medium frequency semicircle is attributed to the charge-transfer resistance (R_{ct}), and the slope line represents the Warburg impedance (Z_w) at low frequency, which indicates the lithium-diffusion process within the electrodes.^{42,43} Obviously, the R_{ct} of LVO-PVA/PEO (32Ω) is much smaller than that of LVO-PVA (372Ω) and LVO-PEO (429Ω). The suppression of R_{ct} further confirms that the network structure indeed provides higher efficient electron/ion transport and improves the charge transfer kinetics. The slanted line is attributed to the diffusion of Li ions in the bulk of the electrode material, and the diffusion coefficient value (D) can be calculated from eqn (1) and (2).⁴⁴

$$Z' = R_c + R_{\text{ct}} + \sigma_w \omega^{-1/2} \quad (1)$$

$$D = 0.5(RT/An^2F^2\sigma_w C)^2 \quad (2)$$

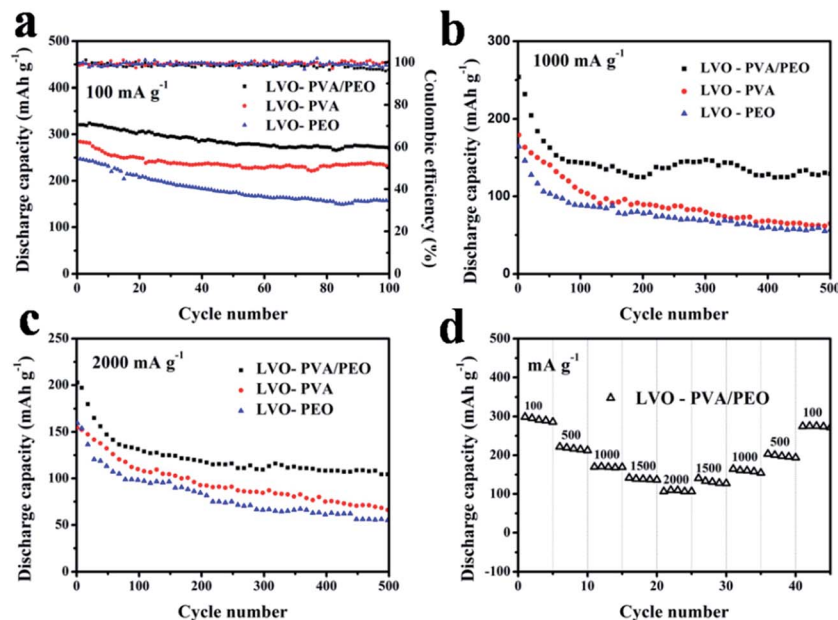


Fig. 7 Electrochemical properties of LVO-PVA/PEO, LVO-PVA and LVO-PEO. The cycling performance at current densities of 100 (a), 1000 (b) and 2000 mA g^{-1} (c), respectively. (d) Rate performance of LVO-PVA/PEO.

In eqn (1), $\omega(2\pi f)$ is the angular frequency in the low frequency region, and both R_e and R_{ct} are kinetics parameters independent of frequency. Then, the Warburg coefficient (σ_w) can be obtained from the slope of the fitting line (Fig. 8b). In eqn (2), R is the gas constant, T is the temperature, A is the area of the electrode, n is the number of electrons transferred per mole of the active material involved in the electrode reaction, F is Faraday's constant and C is the molar concentration of Li ions. The apparent Li ion diffusion coefficients for LVO-PVA/

PEO, LVO-PVA and LVO-PEO based electrodes are calculated to be 2.30×10^{-12} , 1.64×10^{-12} and $0.91 \times 10^{-12} \text{ cm}^2 \text{ s}^{-1}$, respectively, indicating the faster Li ion diffusion ability of LVO-PVA/PEO.

On the basis of the above results, the hierarchical LiV_3O_8 nanowire-in-network exhibits enhanced electrochemical performance. The reasonable explanation is discussed as follows. First, the self-aggregation of small nanorods can be effectively prevented through constructing a hierarchical nanowire-in-network structure, and the well-connected nanowires keep the structure more stable. Second, the width and length of each attached nanorod are around 50 nm and 150 nm, respectively. The small size of the building blocks further realizes the advantages of nanostructured materials and improves the electrochemical performance of the LiV_3O_8 electrode. Finally, the unique structure can provide continuous electron/ion conduction and extra tunnels for efficient contact between LiV_3O_8 and electrolytes compared to a simple nanowire structure. Therefore, the charge transfer kinetics and cycling stability of LiV_3O_8 are promoted.

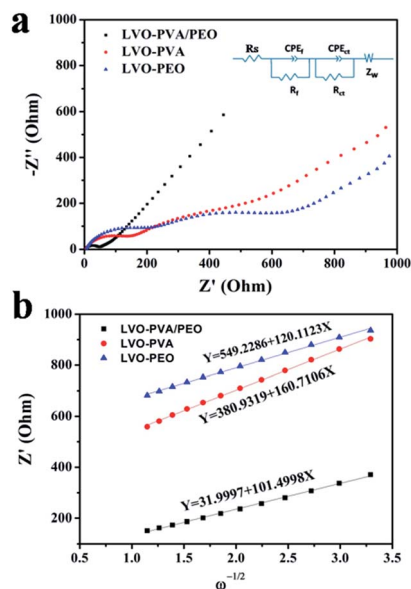


Fig. 8 (a) Nyquist plots of LVO-PVA/PEO, LVO-PVA, and LVO-PEO at 3 V and (b) the relationship curves between Z' and $\omega^{-1/2}$ in the low frequency range.

Conclusions

In summary, we have developed a facile electrospinning method to synthesize a hierarchical LiV_3O_8 nanowire-in-network material. The use of polymer blends (PVA and PEO) is crucial for the formation of the structure. The LVO-PVA/PEO cathode shows excellent electrochemical performance. When cycled at a current density of 100 mA g^{-1} , the initial discharge capacity of LVO-PVA/PEO can reach $320.6 \text{ mA h g}^{-1}$ and it still delivers a capacity of $271.7 \text{ mA h g}^{-1}$ after 100 cycles. More importantly, the LVO-PVA/PEO exhibits outstanding rate performance ($254.0 \text{ mA h g}^{-1}$ at 1000 mA g^{-1} and $202.8 \text{ mA h g}^{-1}$ at 2000 mA g^{-1}). This remarkable performance is attributed to the

hierarchical nanowire-in-network structure, which provides a large effective contact area, low charge transfer resistance and improved structural stability. Our work indicates that the cross-linking strategy in the electrospinning method may be an effective way to construct a unique architecture for high-performance lithium battery applications.

Acknowledgements

This work was supported by the National Basic Research Program of China (2013CB934103, 2012CB933003), the International Science and Technology Cooperation Program of China (2013DFA50840), the National Science Fund for Distinguished Young Scholars (51425204), the Natural Science Foundation of Hubei Province (2014CFA035), the Fundamental Research Funds for the Central Universities (2014-VII-007, 2014-YB-001, 2014-YB-002), and the Students Innovation and Entrepreneurship Training Program (20141049701006). Thanks to Prof. J. Liu of Pacific Northwest National Laboratory and Prof. D. Y. Zhao of Fudan University for strong support and stimulating discussion.

References

- 1 Y. Gogotsi and P. Simon, *Science*, 2011, **334**, 917–918.
- 2 M. Armand and J. M. Tarascon, *Nature*, 2008, **451**, 652–657.
- 3 S. Chu and A. Majumdar, *Nature*, 2012, **488**, 294–303.
- 4 B. Kang and G. Ceder, *Nature*, 2009, **458**, 190–193.
- 5 J. B. Goodenough and Y. Kim, *Chem. Mater.*, 2010, **22**, 587–603.
- 6 A. S. Arico, P. Bruce, B. Scrosati, J. M. Tarascon and W. van Schalkwijk, *Nat. Mater.*, 2005, **4**, 366–377.
- 7 N. A. Chernova, M. Roppolo, A. C. Dillon and M. S. Whittingham, *J. Mater. Chem.*, 2009, **19**, 2526–2552.
- 8 M. S. Whittingham, *Chem. Rev.*, 2004, **104**, 4271–4301.
- 9 C. K. Chan, H. Peng, G. Liu, K. McIlwrath, X. F. Zhang, R. A. Huggins and Y. Cui, *Nat. Nanotechnol.*, 2008, **3**, 31–35.
- 10 B. Scrosati, J. Hassoun and Y. K. Sun, *Energy Environ. Sci.*, 2011, **4**, 3287–3295.
- 11 A. Pan, J. Liu, J. G. Zhang, G. Cao, W. Xu, Z. Nie, X. Jie, D. Choi, B. W. Arey, C. Wang and S. Liang, *J. Mater. Chem.*, 2011, **21**, 1153–1161.
- 12 A. Pan, J. G. Zhang, G. Cao, S. Liang, C. Wang, Z. Nie, B. W. Arey, W. Xu, D. Liu, J. Xiao, G. Li and J. Liu, *J. Mater. Chem.*, 2011, **21**, 10077–10084.
- 13 D. Sun, G. Jin, H. Wang, X. Huang, Y. Ren, J. Jiang, H. He and Y. Tang, *J. Mater. Chem. A*, 2014, **2**, 8009–8016.
- 14 L. Mai, L. Xu, C. Han, X. Xu, Y. Luo, S. Zhao and Y. Zhao, *Nano Lett.*, 2010, **10**, 4750–4755.
- 15 M. Zhao, B. Zhang, G. Huang, H. Zhang and X. Song, *J. Power Sources*, 2013, **232**, 181–186.
- 16 K. Kim, S. H. Park, T. H. Kwon, J. E. Park, H. Ahn and M. J. Lee, *Electrochim. Acta*, 2013, **89**, 708–716.
- 17 Y. Dong, S. Li, K. Zhao, C. Han, W. Chen, B. Wang, L. Wang, B. Xu, Q. Wei, L. Zhang, X. Xu and L. Mai, *Energy Environ. Sci.*, 2015, **8**, 1267–1275.
- 18 L. L. Liu, X. J. Wang, Y. S. Zhu, C. L. Hu, Y. P. Wu and R. Holze, *J. Power Sources*, 2013, **224**, 290–294.
- 19 R. Mo, Y. Du, N. Zhang, D. Rooney and K. Sun, *J. Power Sources*, 2014, **257**, 319–324.
- 20 S. H. Choi and Y. C. Kang, *Chem.–Eur. J.*, 2013, **19**, 17305–17309.
- 21 R. Mo, Y. Du, N. Zhang, D. Rooney and K. Sun, *Chem. Commun.*, 2013, **49**, 9143–9145.
- 22 H. Wang, Y. Ren, Y. Wang, W. Wang and S. Liu, *CrystEngComm*, 2012, **14**, 2831–2836.
- 23 J. Liu, K. Tang, K. Song, P. A. van Aken, Y. Yu and J. Maier, *Nanoscale*, 2014, **6**, 5081–5086.
- 24 L. Liang, M. Zhou and Y. Xie, *Chem.–Asian J.*, 2012, **7**, 565–571.
- 25 Q. An, Q. Wei, P. Zhang, J. Sheng, K. M. Hercule, F. Lv, Q. Wang, X. Wei and L. Mai, *Small*, 2015, **22**, 2654–2660.
- 26 A. Greiner and J. H. Wendorff, *Angew. Chem., Int. Ed.*, 2007, **46**, 5670–5703.
- 27 C. L. Zhang and S. H. Yu, *Chem. Soc. Rev.*, 2014, **43**, 4423–4448.
- 28 B. Sun, Y. Z. Long, H. D. Zhang, M. M. Li, J. L. Duvail, X. Y. Jiang and H. L. Yin, *Prog. Polym. Sci.*, 2014, **39**, 862–890.
- 29 T. H. Hwang, Y. M. Lee, B. S. Kong, J. S. Seo and J. W. Choi, *Nano Lett.*, 2012, **12**, 802–807.
- 30 X. Xu, Y. Z. Luo, L. Q. Mai, Y. L. Zhao, Q. Y. An, L. Xu, F. Hu, L. Zhang and Q. J. Zhang, *NPG Asia Mater.*, 2012, **4**, e20.
- 31 L. Li, N. Chen and Q. Wang, *J. Polym. Sci., Part B: Polym. Phys.*, 2010, **48**, 1946–1954.
- 32 R. Tossici, R. Marassi, M. Berrettoni, S. Stizza and G. Pistoia, *Solid State Ionics*, 1992, **57**, 227–234.
- 33 L. de Picciotto, K. Adendorff, D. Liles and M. Thackeray, *Solid State Ionics*, 1993, **62**, 297–307.
- 34 K. P. Lee, K. M. Manesh, K. S. Kim and A. I. Gopalan, *J. Nanosci. Nanotechnol.*, 2009, **9**, 417–422.
- 35 A. Koski, K. Yim and S. Shivkumar, *Mater. Lett.*, 2004, **58**, 493–497.
- 36 J. S. Park, J. W. Park and E. Ruckenstein, *Polymer*, 2001, **42**, 4271–4280.
- 37 M. Krumova, D. Lopez, R. Benavente, C. Mijangos and J. Perena, *Polymer*, 2000, **41**, 9265–9272.
- 38 S. A. Theron, E. Zussman and A. L. Yarin, *Polymer*, 2004, **45**, 2017–2030.
- 39 H. G. Wang, D. L. Ma, Y. Huang and X. B. Zhang, *Chem.–Eur. J.*, 2012, **18**, 8987–8993.
- 40 A. Sakunthala, M. Reddy, S. Selvasekarapandian, B. Chowdari and P. C. Selvin, *J. Phys. Chem. C*, 2010, **114**, 8099–8107.
- 41 J. Kawakita, T. Kato, Y. Katayama, T. Miura and T. Kishi, *J. Power Sources*, 1999, **81**, 448–453.
- 42 H. Song, Y. Liu, C. Zhang, C. Liu and G. Cao, *J. Mater. Chem. A*, 2015, **3**, 3547–3558.
- 43 H. Ma, Z. Yuan, F. Cheng, J. Liang, Z. Tao and J. Chen, *J. Alloys Compd.*, 2011, **509**, 6030–6035.
- 44 H. Wang, K. Huang, Y. Ren, X. Huang, S. Liu and W. Wang, *J. Power Sources*, 2011, **196**, 9786–9791.